Formation and Stability of Pb-Sn Embedded Multiphase Alloy Nanoparticles *via* Mechanical Alloying

PATAN YOUSAF KHAN, M. MANOLATA DEVI, and KRISHANU BISWAS

The present paper describes the preparation, characterization, and stability of Pb-Sn multiphase alloy nanoparticles embedded in Al matrix *via* mechanical alloying (MA). MA is a solid-state processing route, which can produce nanocrystalline phases by severely deforming the materials at high strain rate. Therefore, in order to understand the effect of the increasing interface as well as defects on the phase transformation behavior of Pb-Sn nanoparticles, Pb-Sn multiphase nanoparticles have been embedded in Al by MA. The nanoparticles have extensively been characterized using X-ray diffraction and transmission electron microscope. The characterization reveals the formation of biphasic as well as single-phase solid solution nanoparticles embedded in the matrix. The detailed microstructural and differential scanning calorimetry studies indicate that the formation of biphasic nanoparticles is due to size effect, mechanical attrition, and ballistic diffusion of Pb and Sn nanoparticles embedded in Al grains. Thermal characterization data reveal that the heating event consists of the melting peaks due to the multiphase nanoparticles and the peak positions shift to lower temperature with the increase in milling time. The role of interface structure is believed to play a prominent role in determining the phase stability of the nanoparticle. The results are discussed in the light of the existing literature.

I. INTRODUCTION

THE phase transformation behavior of the embedded alloy nanoparticles has widely been investigated in the last two decades.[1–3] Proper understanding of the size effect on the stability in terms of melting and solidification behavior of these alloy nanoparticles is further required to explore the potential applications of these materials. Embedded alloy nanoparticles are considered as a potential material for low-melting temperature solders in printed circuit board (PCB), flip-chip packaging technology, and self-lubricating bearings.[4] Additionally, they are considered as a model system to study the phase transformation and alloying at nanoscale. Thus, scientific understanding of the melting and solidification phenomena needs to be understood to decipher the mechanisms of the melting and solidification. Using the advantages of miscibility gap in the ternary phase diagram (Al-Pb-Sn, Al-Pb-In, Al-Bi-Sn, Al-Cd-Pb, Al-In-Sn, Al-Bi-Sn, *etc.*), various types of multiphase nano-alloy inclusions were prepared by rapid solidification processing (RSP) as well as ion implantation routes.[5–13] These studies conclusively reveal the role of the interface between the phases of the nanoparticles and the matrix, in governing the thermal stability and the phase transformation of the nanoinclusions.[7] Earlier studies also indicate that nanoinclusions prepared by RSP, especially melt spinning, exhibit regular shapes and proper orientation relationship (OR) with the matrix. Thus, the phase transformation behavior can directly be correlated with the interface structure. The interface structure can either be altered by changing the matrix or by processing route. As the matrix is found to play a vital role in governing the thermal stability of the nanoinclusions, even change of matrix can affect the phase transformation behavior of the nano-alloy inclusions.[14,15] For a given matrix, the processing route can also alter the interface structure and thus phase transformation.

Mechanical alloying (MA) is one of the solid-state processing routes involving severe plastic deformation, and hence the formation of different interface structures between the phases in alloy nanoparticles and the matrix is expected.[14] Therefore, MA can effectively be used to study the effect of increased interface on the phase transformation of embedded alloy nanoparticles. It is to be noted that several attempts have been made earlier to understand the phase transformation behavior of nanoinclusions of pure metals like Pb embedded in Al matrix[16–18] and Bi in Ag matrix,[19] prepared using MA. The studies have shown that interface structure plays an important role in deciding the phase transformation of the nanoinclusions. It has also been reported that the nanoparticles exhibit depression in melting point as compared to their bulk values in all the cases. Taking into account the decades of research, it can be inferred

PATAN YOUSAF KHAN and M. MANOLATA DEVI, Ph.D. Students, and KRISHANU BISWAS, Associate Professor, are with the Department of Materials Science and Engineering, Indian Institute of Technology Kanpur, Kanpur 208016, India. Contact e-mail: kbiswas@iitk.ac.in

that the interfaces have a strong influence on phase transformation of embedded metal nanoparticles. However, to the best of the author's knowledge, such kind of study on multiphase alloy nanoparticles embedded in a matrix, prepared using MA, has not been explored yet. Therefore, the formation, structural, and thermal characterization of nano-alloy inclusion is needed to be carried out to understand the thermal behavior of the single- or multiphase alloy nanoparticles embedded in a matrix, prepared *via* MA.

In the present investigation, an attempt has been made to prepare Pb-Sn multiphase alloy nanoparticles in Al matrix by MA of the elemental powders. Al, Pb, and Sn metals have been chosen due to the fact that Al, Pb and Al, Sn have positive heat of mixing, and under equilibrium conditions, there is no solid solubility between Al and Pb and very low (0.026 at.pct) solubility of Sn in Al at room temperature. The obtained nanoparticle powders after MA are characterized by X-ray diffraction (XRD), scanning electron microscopy (SEM), transmission electron microscopy (TEM), and differential scanning calorimetry (DSC). The results obtained are explained using thermodynamics and kinetics of the non-equilibrium process. The formation, morphology, crystallography, and thermal stability are discussed in detail.

II. EXPERIMENTAL DETAILS

A. *Sample Preparation*

Commercially available pure powders (purity of 99.99 pct) of Pb, Sn, and Al with mean particle size of 45, 45, and 35 μm, respectively, have been used for the preparation of the embedded alloy nanoparticles. It is to be noted that Al and Pb have face-centered cubic crystal structure ($Fm\overline{3}m$) with lattice parameter a, 0.404 and 0.495 nm, respectively, whereas β-Sn has body-centered tetragonal crystal structure ($I4_1/amd$), with lattice parameters $a = 0.583$ nm and $c = 0.318$ nm.[20] For preparation of alloy nanoparticles embedded in the Al matrix; a unique strategy has been utilized. Initially, Al-8.9 at.pct Pb and Al-25.4 at pct Sn alloys had been prepared by milling powder mixture of Al and Pb as well as Al and Sn for 20 hours. These two blends (Pb in Al and Sn in Al) had been mixed in right proportion so that powder composition became Al-18 at pct (Pb$_{26}$ Sn$_{74}$) and subsequently ball milled for further 20 hours to prepare Pb-Sn alloy embedded in Al matrix. The samples were collected at an interval of 30 minutes during milling for characterization. The experiments were carried out with tungsten carbide balls in tungsten carbide vials with a ball-to-powder ratio (BPR) of 10:1 and a milling speed of 200 rpm using Fritsch (Pulverisette) P5 planetary ball mill. The experiments had been carried out in the presence of toluene to avoid agglomeration and oxidation during milling.

B. *Characterization*

Phase identification of all the samples has been carried out using Bruker D8 Focus X-ray diffractometer (XRD) with Cu K_α radiation ($\lambda = 0.15402$ nm) at a scan rate of 0.5 deg/min. The peak shift was corrected using Si powder as an external standard. Microstructural and compositional analysis has been carried out using scanning electron microscope (SEM, Carl Zeiss EVO 50), attached with an energy-dispersive spectrophotometer (EDS, INCAPENTA FET ×3), operated at 20 kV. Fine-scale microstructural characterization had been carried out using transmission electron microscope (TEM, Tecnai UTWIN 20) operated at 200 kV. The melting and solidification behavior of the nanoparticles was studied using differential scanning calorimeter (TGA/DSC, Mettler Toledo DSC) employing heating and cooling rate of 20 °C/min with Ar flow of 50 mL/minutes. The lattice parameter has been calculated using Cohen's method, which is a least square method.[21] The uncertainty in the lattice parameter measurements was ±0.0005 Å. Hall–Williamson method was employed to find out the crystallite size and root mean square (rms) strain.[22] The formula used is given by

$$\beta \cos \theta = \frac{k\lambda}{d} + 4\varepsilon \sin \theta, \qquad [1]$$

where β is the full width at half maxima, ε is the rms strain, K is a constant which value is assumed to be 0.9, λ is the wavelength of the X-ray (0.15402 nm), d is the crystallite size, and θ is the scattering angle. By plotting $\beta \cos \theta$ Vs $\sin \theta$, one can estimate the values of both ε and d.

III. RESULTS

A. *X-ray Diffraction (XRD)*

Figure 1 shows the XRD patterns of the ball milled powders collected at different times. The diffraction peaks in the XRD patterns (Figure 1(a)) can consistently be indexed due to FCC Pb, BCT β-Sn, and FCC Al. Peaks corresponding to impurities such as oxides, nitrides, *etc.*, could not be detected within the resolution limit of the XRD detector. The magnified views of $(200)_{\beta\text{-Sn}}$, $(101)_{\beta\text{-Sn}}$, and $(111)_{Pb}$ peaks are presented in (Figure 1(b)) for more clarity on the peak positions as a function of milling time. It is to be noted that the peak positions of pure Sn and Pb particles embedded in Al (0 hours milled) are represented by green and red dotted lines, respectively. On careful observation, one can clearly observe that the peak positions of Pb and Sn in the XRD patterns of the powders ball milled for 5 minutes to 20 hours shift to higher angle (2θ) as compared to those of pure Sn and Pb particles embedded in Al (0 hour milled). However, it is to be noted that the extent of peak shifts differs as a function of milling time. The shift in the individual peak positions can be utilized to obtain change in the lattice parameters of Pb and Sn as a function of milling time.

Figures 2(a) and (b) show the change in the lattice parameter (represented as $\Delta a/a_0 \times 100$ pct where as $\Delta a = a - a_0$) as a function of milling time. It can be noticed that the change in the lattice parameter for Pb exhibits decreasing trend as compared to that of the
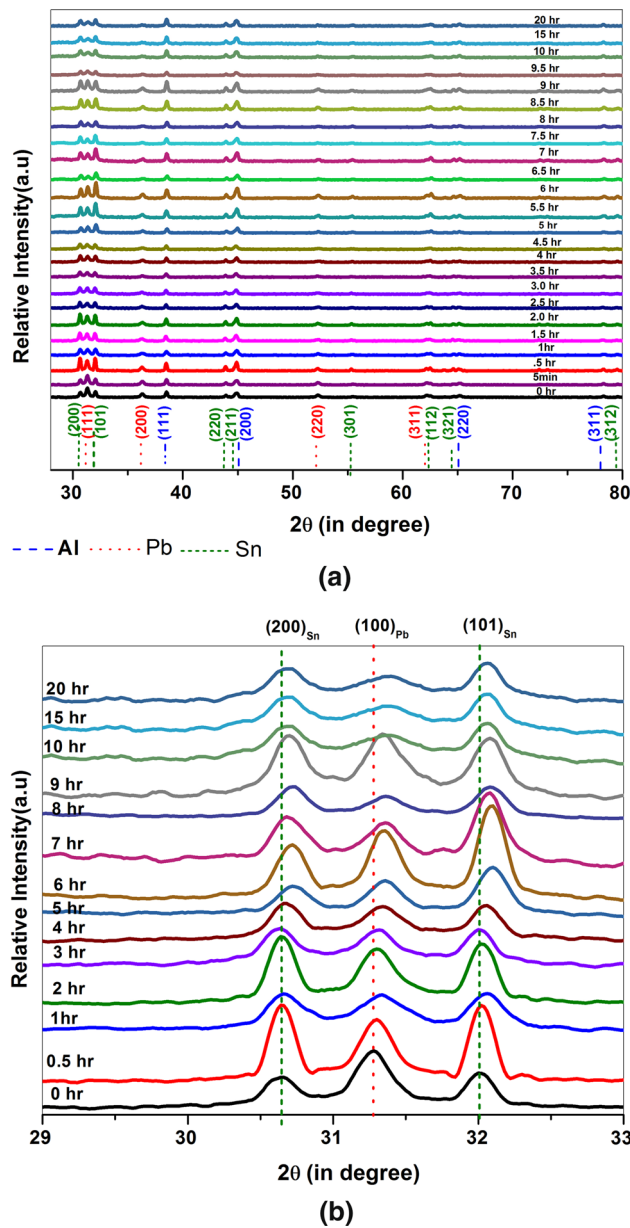
Fig. 1—(a) XRD patterns of the powder samples of Al-18 at.pct $(Pb_{26} Sn_{74})$ milled for different time durations; (b) the magnified views of (200) and (101) peaks of Sn and (111) peak of Pb.

Fig. 2—The variation in lattice parameters with milling time: (a) Pb and (b) Sn.

corresponding 0-hour ball milled powder. For β-Sn, one needs to consider the changes in both a and c of the body-centered tetragonal unit cell. Figure 2(b) shows the changes of a and c ($\Delta a/a_0 \times 100$ pct), ($\Delta c/c_0 \times 100$ pct) as a function of milling time. The similar trend of the lattice parameters with milling time has been observed for Sn also.

In addition, the peaks of Pb, Sn, and Al show substantial broadening as a function of milling time. The peak broadening is more prominent in case of Pb and Sn than Al. The peak broadening can be used to estimate the crystallite size and the rms strain. These two parameters have been calculated using Hall–Williamson method[22] and plotted against milling time (Figures 3(a) and (b)). The calculated crystallite size of Pb and Sn has
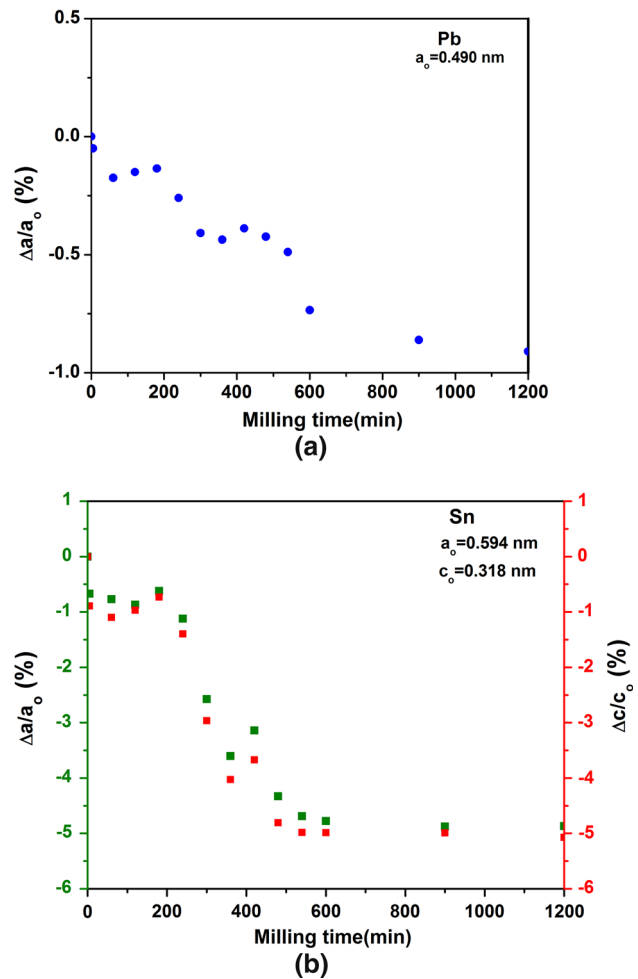
been found to be decreasing from 41 to 17 and 43 to 21 nm, respectively, as the milling time increases from 0 to 20 hours. The rms strain for both Pb and Sn shows an increasing trend as a function of milling time, reaching 0.72 and 0.7 pct, respectively, at 20 hours of ball milling.

B. *Microstructural Characterization of the Ball Milled Powders*

It has been reported[16,18,19] that ball milling of powder involves repeated deformation, welding, fracture, and re-welding of the powder constituents. Therefore, to study the change in morphology of the powder during ball milling, the microstructural characterization has been carried out using SEM. Figures 4(a) through (e) show the representative SEM micrographs obtained from the powders ball milled for 0, 5, 10, 15, and 20 hours, respectively, in the back-scattered electron imaging (BSE) mode to distinguish different phases present in the microstructure.

Figure 4(a) shows the microstructure of the starting powders consisting of blends of Al-8.9 at.pct Pb and Al-25.4 at.pct Sn with irregular-shaped particles having size ranging from 10 to 50 μm. The insets in (Fig-
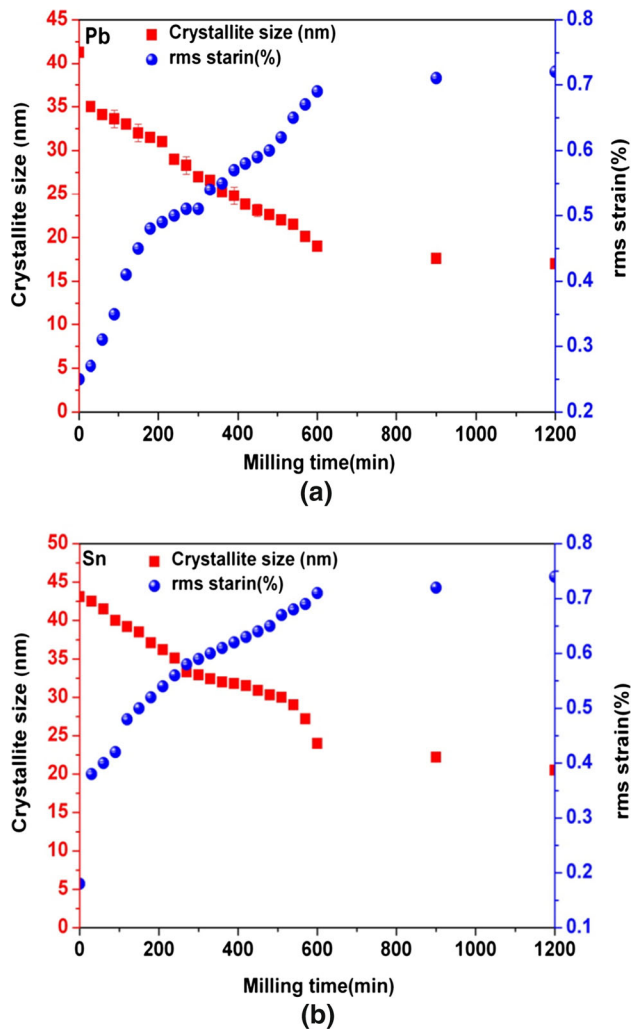
Fig. 3—The variation in crystallite size and rms strain with milling time: (*a*) Pb and (*b*) Sn.

ure 4(a)) show the BSE images of the powder blends of Al-Pb (left inset) and Al-Sn (right inset), showing uniform distribution of Pb and Sn in Al matrix (marked by arrows in the respective image). After 5 hours of milling (Figure 4(b)), the microstructure reveals that the powder particles consist of agglomerated lamellae of Al/Pb/Sn phases. The inset in (Figure 4(b)) shows one such lamella. Further increase in milling time up to 15 hours causes the reduction in the particle size. The representative BSE images of powder samples obtained after 10 and 15 hours are shown in (Figures 4(c) and (d)), respectively. The atomic number contrast reveals the trapping of Pb and Sn particles within Al layers [inset of Figures 4(c) and (d)]. The particles are observed to be uniformly distributed in Al layers. Figure 4(e) shows the BSE image of the 20-hour milled powder. The uniform compositional contrast of embedded particles suggests the formation of Pb-Sn alloy (shown as right inset). The compositional analysis using EDS (as shown in the left inset) shows the presence of Al, Pb, and Sn distinctly. This indicates that Pb and Sn are embedded in Al.

To elucidate the fine-scale microstructure, *i.e.,* morphology, size, and OR of the different phases present in the milled powders, TEM investigations have been carried out extensively. The detailed TEM analysis of the powder has been presented in Figures 5 through 7.

Figure 5(a) is a high-angle annular dark-field (HAADF) image obtained from 20-hour ball milled powder sample. It is to be noted that HAADF provides Z-contrast image. The inset of (Figure 5(a)) shows the higher magnification image revealing nanoparticles with typical two-phase contrast as well as single-phase contrast as marked in the Figure. The corresponding bright-field TEM micrograph is also shown in (Figure 5(b)). The micrograph reveals the presence of the nanometer-sized particles embedded in the nanometer-sized Al grains. The grain size measurements indicate that the average grain size of Al is 50 ± 5 nm. The nanoparticles of Pb-Sn are observed to be uniformly distributed in the Al grains (inset in Figure 5(b)) with an average grain size being 15 ± 5 nm. They do not show any specific shape; rather they exhibit *irregular* morphology. Figure 5(c) reveals the selected area diffraction (SAD) pattern obtained from large number of Al grains having embedded nanoparticles. The careful analysis of diffraction rings reveals the presence of FCC Pb, BCT β-Sn, and FCC Al phases. Thus, it confirms the embedding of the nanoparticles in the Al grains. The detailed microstructural analysis of the individual nanoparticles clearly reveals the presence of two types of the embedded nanoparticles; two phase and single phase. Figures 6(a) and (b) show a pair of bright- and dark-field images of a single-phase nanoinclusion. The SAD pattern obtained from this nanoinclusion [shown in Figure 6(c)] indicates that it is due to Pb. The compositional analysis, carried out using EDS detector, reveals the presence of Pb and Sn in the atomic ratio of 2.5:1. Thus, it is a Pb-rich solid solution phase, (Pb). In addition, it has also been observed that the nanoparticles of (Pb) exhibit near-spherical morphology but fewer in number as compared with the two-phase nanoparticles. The two-phase nanoinclusions exhibit two type of morphologies: irregular [shown in the inset of Figure 5(a)] and lamellar. Figure 7 shows an embedded nanoparticle showing lamellar morphology, which is typically observed in the melt-spun sample.[11,14,15,23] The dark-field micrograph (Figure 7(b)) obtained with (200)_{Sn} reflection further confirms the formation of the biphasic nanoparticles. In order to elucidate the nature of interface between the phase and the matrix, composite SAD patterns obtained from the phase in the nanoparticles along the matrix have been extensively analyzed to get OR. The detailed diffraction pattern analysis from large number of nanoparticles indicates that there is no specific OR being observed among the phases and the matrix. The result is in consistent with the reported literature.[16] However, few biphasic nanoparticles exhibit OR with the matrix. The composite SAD patterns obtained from different phases in lamellar nanoparticle along matrix are shown in (Figures 7(c) and (d)). The patterns can be indexed using the reflections of Al, Pb, and β-Sn. The careful analysis of the SAD patterns indicates the possible OR.
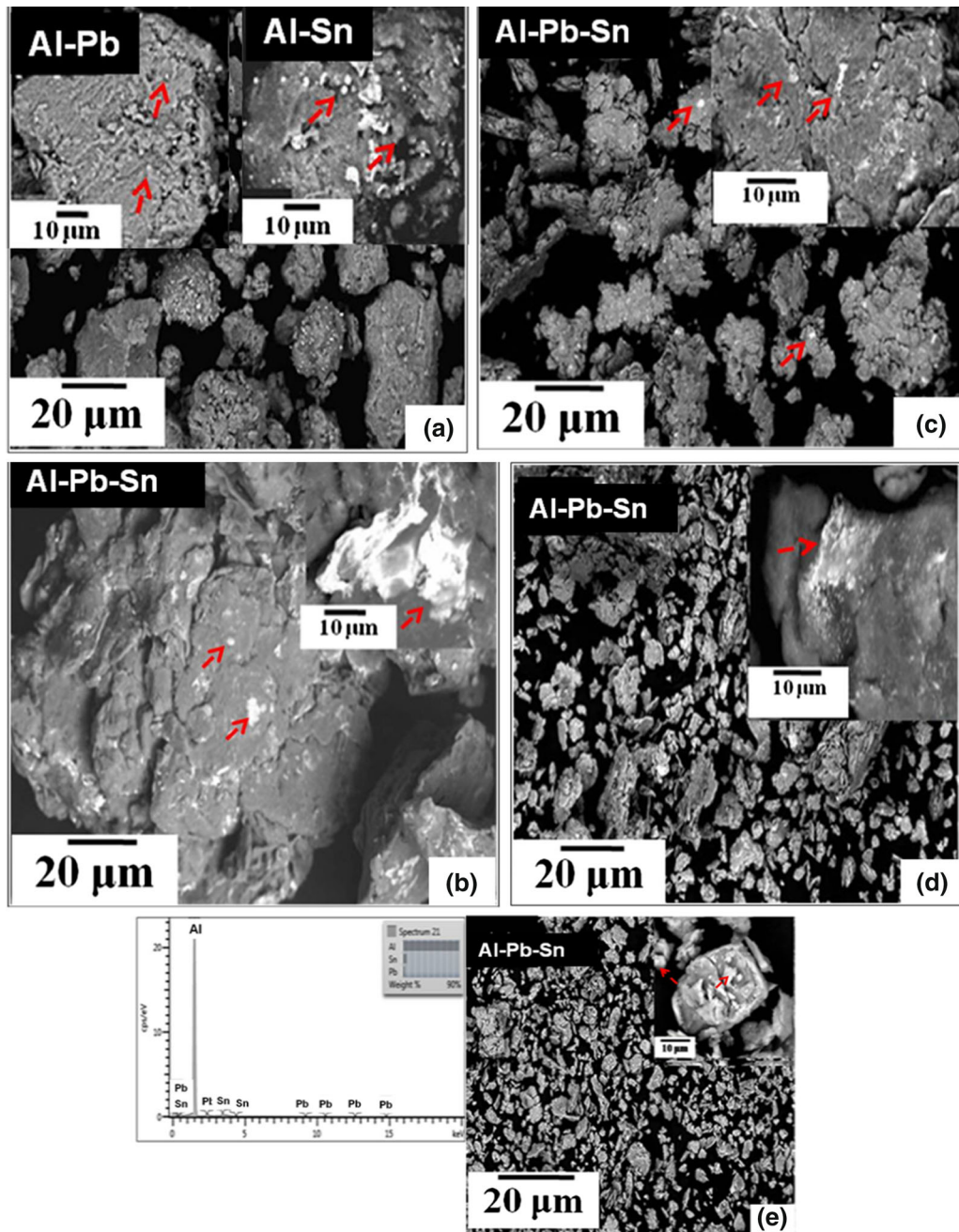
Fig. 4—BSE images of Al-Pb-Sn milled samples for durations: (*a*) 0 h, (*b*) 5 h, (*c*) 10 h, (*d*) 15 h, and (*e*) 20 h. The arrows in the left inset of (a) represent Pb particles, whereas in the right inset arrows represent Sn particles in Al grains. The arrows in the figures (b, c, d, e) represent Pb-Sn particles in Al grains. The EDS pattern in the left inset of e shows the presence of Al, Pb, and Sn in the milled sample.

$$(\bar{1}10)_{Al}//(111)_{Pb} \text{ and } [00\bar{1}]_{Al}//[01\bar{1}]_{Pb}$$

$$(\bar{1}10)_{Al}//(\bar{2}00)_{Sn} \text{ and } [00\bar{1}]_{Al}//[001]_{Sn}$$

The OR is quite different from what has been observed in the melt-spun samples as well as ion-implanted specimen of Pb and Sn nanoparticles embedded in Al matrix.[5–11] In fact, the observed OR is distinctly different from that of the reported individual Pb and Sn nanopar-

ticles embedded in Al.[24–26] The detailed calculation of interplanar spacings (d_{sp}) of different planes ($d_{sp}^{Al(\bar{1}10)} = 0.286$ nm, $d_{sp}^{Pb(11\bar{1})} = 0.283$ nm, $d_{sp}^{Sn(200)} = 0.297$ nm) indicates that d-spacings vary and therefore the interfaces cannot be considered to be coherent. OR does not involve the closed packed planes of Al and Sn, and thus the interfaces between Pb and Al as well as Sn and Al are not low-energy interfaces.

Thus, it is clear that MA leads to the formation of distinctly different interface between the phases in the nanoparticles and the matrix. Therefore, in general, it
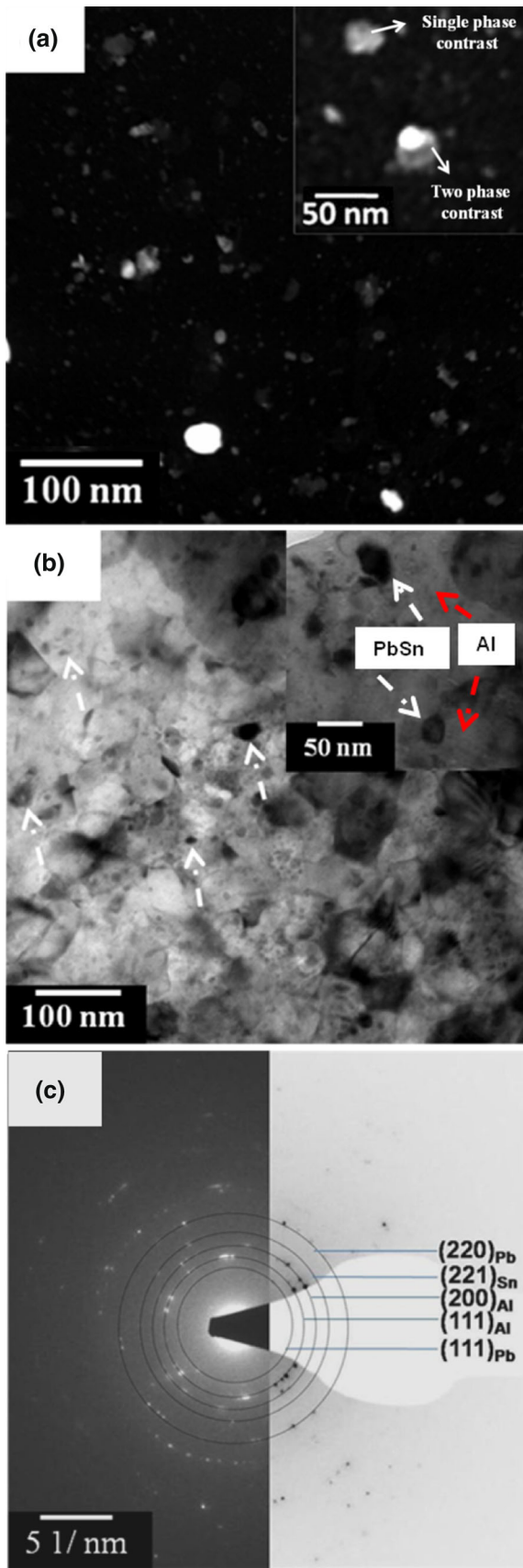
Fig. 5—(a) HAADF image confirms the presence of Pb-Sn particles in Al grains. High-magnification inset shows the presence of biphasic and single-phase nanoparticles; (b) TEM bright-filed image showing the homogeneous distribution of second-phase particles in Al matrix with the inset showing the nanoparticles in Al matrix; (c) The selected area diffraction pattern collected from sample showing the presence of polycrystalline Al, Pb, and Sn phases in the sample.

can be considered not to be coherent or even semi-coherent.

C. Thermal Characterization

To get further insight into the evolution of the microstructure of Al-Pb-Sn MA powder samples during ball milling and the thermal stability of the phases, extensive thermal characterization has been carried out using DSC in the temperature range of 303 K to 673 K (30 °C to 400 °C) at a heating/cooling rate of 20 °C/min. Figure 8 shows the thermograms corresponding to the heating cycle of powders, milled for different durations. The initial powder, a physical mixture of Al-Pb and Al-Sn, reveals two endothermic peaks corresponding to the melting temperature of the nanocrystalline Pb and Sn. The peak positions for Pb and Sn are marked as 1 and 2, respectively, in the figure.

As the milling time increases, the peaks corresponding to both Sn and Pb undergo shift. In case of Sn, the peak shifts to lower temperature. The Pb peak also shifts to lower temperatures up to 6 hours of milling. Beyond 6 hours, this peak is infinitesimally small to be detected. The peak corresponding to Sn is observed to be broaden with milling time. Most importantly, one can detect the appearance of a new peak in the DSC thermograms of powders ball milled for 1 hour and beyond. The intensity of this peak increases with the progress of milling. In fact, the prominent peak observed for 15-hour ball milled powder can be related to the melting of biphasic nanoparticles. This peak is marked as 3 on Figure 8. The details of DSC results for the melting events of the powder specimens are tabulated in Table I. The results will be discussed later.

The cooling curves for Al-Pb-Sn powder samples ball milled for different times are shown in Figure 9. They reveal a number of diffuse and broad peaks. In fact, in some cases we observe multiple peaks. Some of the peaks are marked in the figure. This feature is distinctly different from what has been observed for Al-Pb and Al-Sn ball milled powders, in which the distinct solidification peaks have been observed during cooling (supplementary file). This kind of DSC thermogram clearly indicates that the solidification takes place over a large temperature range. In fact, the typical area under the melting peaks (Figure 8) is much higher than the total areas of the peaks in the cooling thermograms for a specific specimen. This also confirms the solidification indeed taking place over a large temperature range. Generally, the nucleation of solid phase, i.e., solidification, is very sensitive to the presence of nucleation site and the type of impurity.[27] As MA is a severe plastic
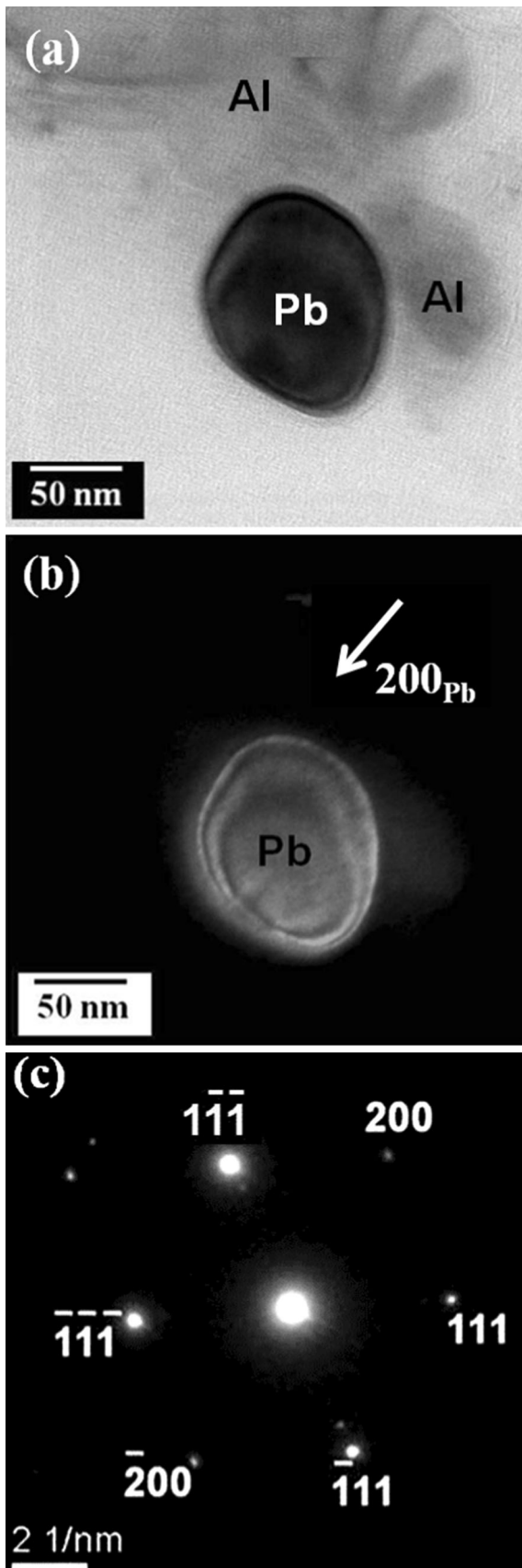
◀ Fig. 6—(*a*) Bright-field TEM image with a single-phase nanoparticle of (Pb) inside the Al grains; (*b*) dark-field image obtained by (200)$_{Pb}$; and (*c*) SAD pattern obtained from the particle indicating the (Pb) phase.

deformation processing technique, there can exist a number of possible nucleation sites due to various defects generated in solid matrix surrounding the nanoparticles by MA. In addition, the impurities coming from the milling media, balls, and vials will also be present. The presence of large number of nucleation sites will catalyze the nucleation of solid during solidification, resulting in the solidification of molten nanoparticles in large temperature range depending on the catalytic efficiency.

IV. DISCUSSION

A. *Formation of Alloy Nanoparticles*

In the present investigation, single-phase as well as two-phase Pb-Sn nanoparticles have systematically been embedded in Al matrix by milling the mixture of Al-8.9 at.pct Pb and Al-25.4 at.pct Sn blends in a high-energy ball mill for 20 hours. The XRD, DSC, and TEM analyses on starting powder blends of Al-8.9 at.pct Pb and Al-25.4 at.pct Sn show that Pb and Sn nanoparticles are embedded in Al matrix after 20 hours of ball milling (supplementary file). Further ball milling of these blends leads to extensive refinement of the microstructure. This has been reflected by extensive broadening of XRD peaks of the Al, Pb, and Sn with milling time. As shown in (Figures 3(a) and (b)), the average crystallite sizes of Pb and Sn can be reduced to 17 and 21 nm, respectively, from about 45 μm. The Al grains also undergo extensive refinement during ball milling. Thus, this allows forming nanocomposite consisting of nanocrystalline Pb or Sn embedded in the nanocrystalline Al grains. This requires explanation, because of the fact that the formation of critical-sized individual nanoparticles is prerequisite for alloy formation. The refinement of grains of ductile metals by means of plastic deformation (ball milling) has attracted extensive attention in the past decades. The structural refinement covers many length scales, from micrometer to ultrafine to even nano range. According to Fecht,[28] grain refinement by MA can occur in three stages. In the first stage, severe plastic deformation is applied to the powder, leading to the formation of shear bands due to repeated and localized deformation. The shear bands, having a high density of dislocation networks, lead to an increase in the plastic strain. The next stage generally involves the formation of sub-grains separated by low-angle grain boundaries due to the arrangement of dislocations in comparatively low-energy configurations. This happens mainly due to the process of annihilation and recombination of the dislocations.[29] In the last stage, the repeated deformation causes the formation of additional shear bands with further reduction of the sub-grains and reorientation of
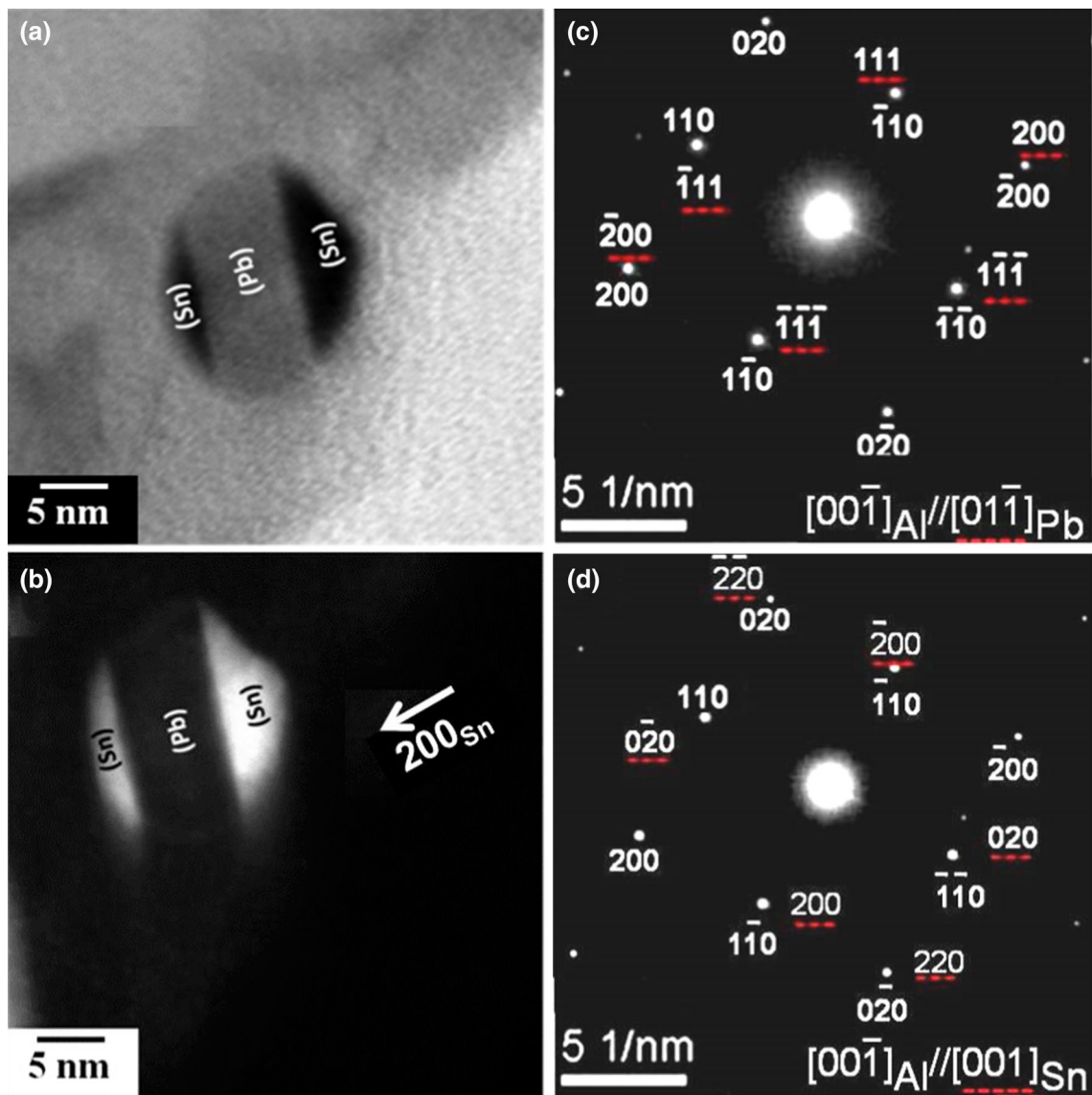
Fig. 7—(a) Bright-field TEM image showing a typical two-phase nanoparticle consisting of Pb and Sn phases; (b) corresponding dark-filed image obtained using $(200)_{Sn}$; and composite SAD patterns collected by (c) including Pb and Al and (d) Sn and Al matrix.

the small-angle grain boundaries. Therefore, the generation, accumulation, and annihilation of dislocations are bare necessities of the grain refinement. In ball milling process, it would be possible to achieve a minimum grain size for the ductile materials due to balance of formation and arrangement of the defects. Thus, the minimum grain size attainable during mechanical milling is decided by the balance between defect generation by plastic deformation and recovery by thermal process. The most comprehensive model for describing the minimum crystallite size obtained during ball milling is due to Mohamed.[29] The minimum grain size is given by

$$\frac{d_{min}}{b} = A\left(\exp\left(\frac{-\beta Q}{4RT}\right)\right)\left\{\frac{D_{po}Gb^2}{v_o kT}\right\}^{0.25}\left(\frac{\gamma}{Gb}\right)^{0.5}\left(\frac{G}{H}\right)^{1.25},$$

[2]

where d_{min} is the minimum crystallite/grain size, D_{po} is the diffusion coefficient for pipe diffusion, G is the shear modulus, b is the magnitude of Burgers vector, v_o is the Poisson's ratio, H is the hardness, k is the Boltzmann constant, Q is the activation energy for thermal recovery, γ is the stacking fault energy, R is the universal gas constant, β is the constant, and T is the absolute temperature. Except T, other parameters are system dependent. It is important to know the temperature of milled powder during milling to calculate d_{min} for individual constituents of the powder.

The ball milling has been carried out at room temperature (RT). During milling, it is likely that temperature would increase due to high-energy impact of the ball. It has been shown by Miller et al.[30] that the local temperature can substantially be increased during milling. In the present case, the temperature of the

powder could not be experimentally determined during the course of ball milling; however, it is possible to estimate theoretically. Schwarz and Koch[31] have analyzed the temperature rise resulting from the localized shear of the powder entrapped between the balls during milling. The following expression provides the temperature rise (ΔT):

$$\Delta T = \frac{F}{2}\left(\frac{\Delta t}{koCp\varPi\rho}\right)^{1/2}, \qquad [3]$$

where F is the dissipated energy flux = $\sigma \cdot V$, σ is the normal stress caused by head-on collision, V is the relative velocity of ball before impact, Δt is the stress state life time, ρ is the powder density, k_o is the thermal conductivity, and C_p is the heat capacity of the powder. By assumption, the normal stress is the maximum compressive stress generated by a head-on collision of the two balls of diameter d,

$$\sigma = \sigma_c = 0.616PE^2\left(\frac{2}{d}\right)^{2/3}, \qquad [4]$$

where P is the load and E is the elastic modulus of the balls. Using the numerical values provided in Table -
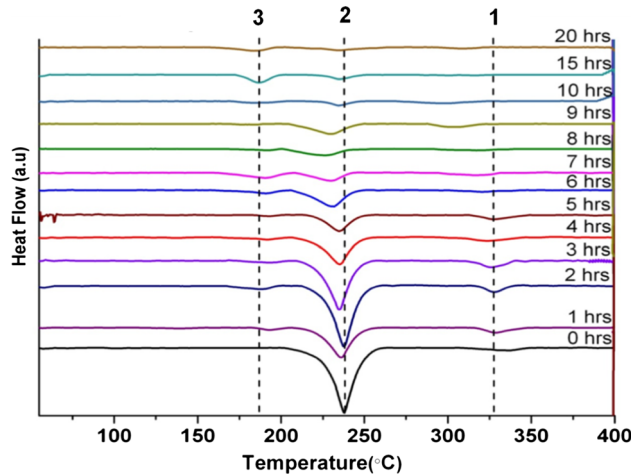
II[31–34] $\Delta T = 475$ K (202 °C). Thus, the temperature of the powder is calculated by $T = RT + \Delta T = 27 + 202 = 229$ °C (502 K). Using $T = 502$ K (229 °C), the calculated values of d_{min} of Al, Pb, and Sn are 12, 16, and 19 nm, respectively. Thus, the calculated values of the grain size of different phases are close to the experimentally measured average grain sizes. Thus, 40 (20 hours of initial powder milling to form Al-Pb and Al-Sn, 20-hour milling of blends of Al-Pb and Al-Sn) hours of ball milling is sufficient to obtain minimum grain/crystallite size.

It is to be noted here that the generation of critical-sized pure nanoparticles is the prerequisite for the formation of embedded alloy nanoparticles.[35,36] As the achieved size of the nanoparticles matches with the theoretical calculations, the formation of alloy nanoparticles will now be discussed in the context of ballistic diffusion of Pb and Sn within the grain of Al and size effect. It is a well-known fact that Pb does not have any solid solubility in Al, whereas Sn has limited solid solubility in Al (0.026 at.pct 625 °C) under equilibrium conditions.[37] Since MA is a non-equilibrium process, it is likely that solid solubilities of Pb and Sn in Al would increase substantially during MA. It has already been reported that Al and Pb have been found to form

Fig. 8—DSC traces during heating of Al-Pb-Sn powders ball milled for different time durations.
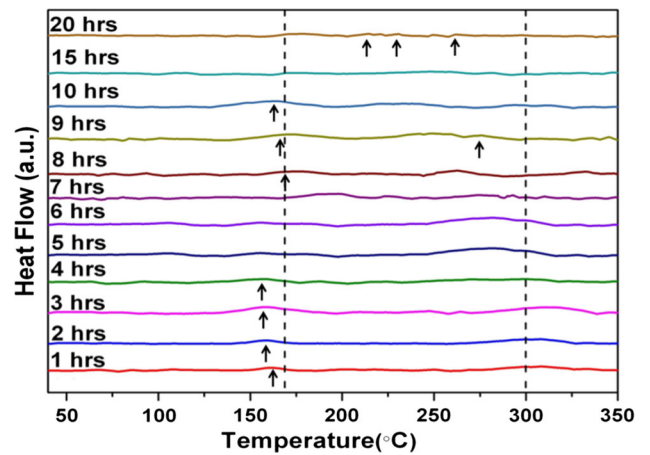

Fig. 9—DSC traces during cooling of Al-Pb-Sn powders ball milled for different time durations.

Table I.   DSC Data of Al-Pb-Sn Milled Samples for Different Time Durations

Milling Time (h)	3rd Peak Temperature [K (°C)]	2nd Peak Temperature [K (°C)]	1st Peak Temperature [K (°C)]
0	NP	505.7 (232.7)	600.3 (327.3)
1	463.6 (190.6)	504.2 (231.2)	599.2 (326.2)
2	463.3 (190.3)	504.0 (231.0)	598.7 (325.7)
3	463.1 (190.1)	501.4 (228.4)	598.7 (325.7)
4	460.0 (190.0)	500.8 (227.8)	598.3 (325.3)
5	462.4 (189.4)	498.6 (225.6)	598.2 (325.2)
6	459.5 (186.5)	497.2 (224.2)	NP
7	459.1 (186.1)	496.5 (223.5)	NP
8	459.0 (186.0)	502.8 (229.8)	NP
9	459.5 (186.5)	501.4 (228.4)	NP
10	456.0 (183.0)	492.0 (219.0)	NP
15	452.5 (179.5)	491.9 (218.9)	NP
20	452.4 (179.4)	491.7 (218.7)	NP

The melting points of different phases mentioned in table (*NP not present).

Table II. Values of Different Parameters Used in the Calculation of Temperature Rise as Well as the Minimum Particle Size Obtained During Ball Milling

|	
Thermal conductivity, K_{Al}	237 w/m K[24]
Relative Velocity, V_r	2.5 m/s[30]
Tungsten carbide balls density, ρ_b	11320[34]
Specific heat, $C_{p\ Al}$	900 J/Kg K[29]
Diameter of WC balls, d	0.01 m
Longitudinal wave velocity of WC balls, Vs	6220 m/s[31]
Density, $\rho_{Al},\ \rho_{Pb},\ \rho_{Sn}$	2710, 11,320, 7290 kg/m³[32]
Boltzmann constant, k	0.0083144 kJ/mol K
Gas constant, R	0.0083 kJ/mol K
Temperature	475 K (202 °C)
Shear modulus (G) Al, Pb, Sn	26 GPa [26], 6 Gpa [26], 18 GPa [31]
Burger vector (b) Al, Pb, Sn	0.2863, 3500 nm [26], 0.3172 nm [31]
Poison ratio (v_0) Al, Pb, Sn	0.345, 0.44 [26], 0.37 [31]
Vickers Hardness (Hv) Al, Pb, Sn	0.167, 0.088, 0.088 GPa [31]
β	0.04 [26]
Stacking fault energy (γ) Al, Pb, Sn	200 mJ/m² [26], 25 mJ/m² [32], 3 mJ/m² [32]
Self diffusion coefficients (Dp_0) Al, Pb, Sn	0.176, 0.995, 12.8 cm²/s [33]
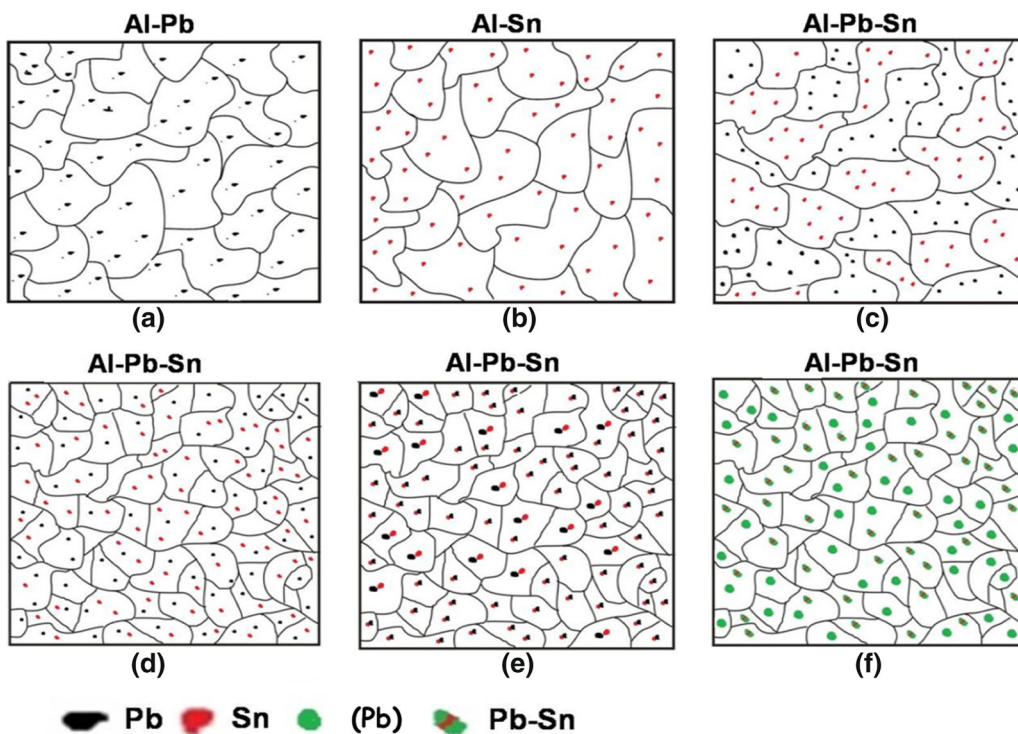
Fig. 10—Schematic diagrams showing the mechanism of the formation of single-phase and biphasic alloy nanoparticles of Pb-Sn in Al during mechanical alloying. (*a*) and (*b*) represent Pb and Sn nanoparticles embedded in Al, respectively; (*c*) mixture of Al-Pb and Al-Sn blends; (*d*), (*e*), and (*f*) representing the formation of alloy nanoparticles in Al matrix.

supersaturated Al(Pb) solid solution during high-energy mechanical milling even though they have positive heat of mixing.[38–40] In addition, it has also been reported that the sizes of the embedded Pb nanoparticles in Al[41] and embedded Bi nanoparticles in Al-Cu-Fe,[42] which are well-known immiscible systems, have also been found to be increased during fretting wear test. These are reported to be due to pipe diffusion, *i.e.*, particles are interconnected by dislocations and they can have diffusion through dislocations.[41] These experimental evidences clearly indicate that during mechanical working or friction, mutual solid solubility of immiscible system

can be increased substantially. The mechanisms responsible for the increase of solid solubility in immiscible system have been proposed to be consisting of two factors: (a) atomic mixing due to continuous shearing of atomic planes during milling-induced plastic deformation, *i.e.*, ballistic diffusion, and (b) interdiffusion of the constituent elements that can increase substantially when the size of particle becomes lesser than a critical size.[43] Thus, the solubility of Pb and Sn in Al is expected to be increased substantially during MA due to the combined effect of defect-induced diffusion (ballistic diffusion) and size effect. Once Pb and Sn come in contact with each

other within nanocrystalline grains of Al, they can either form (Sn) or (Pb) nanoparticles or two-phase nanoparticles depending on the relative availability of the alloying elements due to size effect and ballistic diffusion as well as rise in temperature during MA.

The ballistic diffusion coefficient (D^b) for both Pb and Sn nanocrystals can be estimated using a model due to Bellon and Averback.[44] It is given by

$$D^b = \frac{\Gamma}{2} P^2, \qquad [5]$$

where $\Gamma = \frac{\gamma_{Sn}}{N}$ and $P^2 = a^2$ for Pb and $P^2 = a^2 + c^2$ for Sn, where a and c are lattice parameters. γ_{Sn} is known as shear rate, and N is the number of unit cells of Pb or Sn present in a typical powder particle. For a powder size of 1 μm, $N = 10^4$. It is extremely difficult to estimate γ_{Sn} from ball mill parameters. As pointed out by Bellon and Averback,[36] γ_{Sn} ranges from 1 to 10^5 s^{-1}. Using an average value of $\gamma_{Sn} = 10^3$ s^{-1} and $N = 10^4$ and lattice parameters of Pb and Sn, one can obtain ballistic diffusivities as $D^b_{Pb} = 4.08 \times 10^{-20}$ m^2/s and $D^b_{Sn} = 7.35 \times 10^{-20}$ m^2/s.

Figure 10 schematically shows the process of solid-state diffusion leading to the formation of such alloy nanoparticles. During the MA process, the reduced crystallites of Pb and Sn come in contact with Al grain boundaries by mechanical attrition. The rise in temperature during MA will provide driving force for diffusion of the Pb and Sn grains into Al grain. The atoms of Pb and Sn from nanoparticles embedded in Al grains can diffuse and react to form the biphasic nanoparticle, provided that the alloy composition falls within the coupled zone of Pb. The width of the coupled zone in Pb-Sn system has been well established.[45–47] Xie et al. calculated the wide composition range (43 to 78 wt pct Sn) in which coupled zone can exist in Pb-Sn alloy.[48] One can even make an effort to calculate the time required for diffusion only. Let us assume that Pb and Sn nanoparticles are in the same Al-grains. The average grain size of Al is 15 nm. The time required for Pb atoms to move to Sn sitting on opposite grain boundary in an Al grain or vice versa can calculated using the diffusivity of Pb in Al or Sn in Al. The diffusivity of Pb in Al is reported to be (D_{Pb}) 1.54×10^{-16} m^2/s[29] whereas that of Sn in Al[49] is (D_{Sn}) 17.1×10^{-16} m^2/s. Thus, time required for Pb atoms to move to Sn atoms is estimated to be $t = 0.36$ seconds. Similarly, the time required for Sn atoms to move to Pb atom is $t = 0.13$ seconds. Therefore, the formation of biphasic nanoparticles can also be justified by diffusional arguments.

B. Stability of Nanoparticles

We shall finally discuss the stability of Pb-Sn alloy nanoparticles embedded in the Al matrix processed by MA with the help of DSC studies during heating. It is to be noted that the melting of the nanoparticles (free and embedded) has extensively been researched upon over the last few decades.[1–3] It is well known that the melting of the nanoparticles is size dependent.[50] The free nanoparticles reveal the lowering of the melting temperature,

while embedded ones exhibit superheating as compared to the equilibrium melting temperature.[1–3] Generally, the nature of interface is thought to play a key role in determining the melting behavior.[2] This behavior can also be related to the shape of the nanoparticles, the epitaxy between the nanoparticle and the matrix, and the associated pressure effect by the matrix in the embedded nanoparticles.[51] In the present case of pure Pb or Sn nanoparticles embedded in Al matrix, the melting point depression has been observed (supplementary file). It is to be noted that similar trend has been found in the reported literature.[16] This depression in the melting temperature can be explained with the help of classical thermodynamical approach. The ratio of the melting temperature of an embedded nanoparticle of radius r to the bulk melting temperature is given by[2]

$$\frac{T_m(r)}{T_0} = 1 - \frac{3}{rL_m\rho_s}\left[\gamma_{sm} - \gamma_{lm}\left(\frac{\rho_s}{\rho_l}\right)^{2/3}\right] + \frac{\Delta E}{L_m}, \qquad [6]$$

where ρ_s and ρ_l are the densities of solid and liquid nanoparticles, respectively, L_m is the latent heat, γ_{sm} and γ_{lm} are the interfacial energies of solid particle/matrix and liquid particle/matrix interfaces, respectively, ΔE is the change in the strain energy, and r is the radius of the nanoparticle. The contribution of ΔE mainly originates from differential thermal expansion of the matrix and particle on melting. According to the equation, superheating or depression of melting temperature will depend on the relative values of γ_{sm} and γ_{lm} provided $\rho_s = \rho_l$ In case $\gamma_{sm} < \gamma_{lm}$, the melting will be promoted and consequently the lowering of melting temperature. As the melting begins, solid particle/matrix interface will be replaced by a solid/liquid interface for the nanoparticle and a liquid/matrix interface for the matrix. Therefore, the melting of the nanoparticle will be governed by excess free energy given by

$$\Delta\gamma = \gamma_{sm} - (\gamma_{sl} + \gamma_{lm}), \qquad [7]$$

where γ_{sl} is the solid-to-liquid interfacial energy of the nanoparticle, γ_{lm} is the liquid—matrix interfacial energy, and γ_{sm} is the interfacial energy between the solid particle and the matrix. Thus, a depression of melting temperature will occur if $\langle\gamma_{sm}\rangle(\gamma_{sl} + \gamma_{lm})$. In case of pure Pb and Sn nanoparticles embedded in Al matrix, the lack of any specific OR between the nanoparticle and the matrix indicates non-coherent nature of the interface. Thus, the melting temperature of Pb and Sn embedded nanoparticles has been found to be depressed. Similarly, in case of the Pb-Sn alloy nanoparticles in Al, no specific OR has been observed, indicating that the interface between the nanoparticle and the matrix is incoherent. However, it is difficult to conclusively say whether the alloy nanoparticles exhibit superheating or depression of the melting temperature. This is because the melting temperature of a solid solution phase will strongly depend on the local composition.

The detailed analysis of the DSC data as presented in Figure 8 as well as Table I reveals that both the first and second peak temperatures shift to lower temperature, indicating a trend that can be treated as depression in

the melting temperature. As indicated earlier in the Section IV–A, the ball milling leads to the formation of alloy nanoparticle of (Pb) or (Sn) depending on the available alloying element as well as Pb-Sn within the Al grains. Melting peak corresponding to the alloy particle is observable after 1 hour of ball milling. This melting peak becomes more clear with the increase in milling time and prominently observed after 15 hours of ball milling, indicating that, with the increase in the milling time, more particles of biphasic alloy nanoparticles form Pb-Sn with composition lying in coupled zone.

For Pb-Sn alloy (single as well as biphasic) nanoparticles, the solidification is found to be diffused. DSC traces consist of multiple peaks. Similar trend has been observed for Pb-Sn alloy nanoparticles in Al or quasicrystalline matrices.[6,23] This may be related to the presence of large number of different nucleation sites present in the sample. As both the (Pb) and (Sn) do not bear any specific OR with Al matrix, the different nanoparticles solidify at different levels of undercooling. In other words, the matrix phase can trigger solidification differently depending on the OR (existing or nonexisting). This aspect will be investigated later in a detailed manner and will be communicated separately.

V. CONCLUSIONS

The present investigation conclusively reveals the possibility of producing biphasic as well as single-phase Pb-Sn alloy nanoparticles embedded in Al matrix *via* MA.

1. The TEM microstructures reveal the formation of biphasic particles of Pb-Sn alloy as well as single solid solution phase of (Pb).
2. Formation of alloy particles is caused by size effect, mechanical attrition, ballistic diffusion of Pb and Sn particles in Al matrix, and temperature rise of powder during ball milling.
3. Thermal characterization results show the trend of depression in melting point of Pb and Sn phases and formation of biphasic alloy particle with the increase in milling time.
4. Solidification is observed to be diffused, indicating the presence of large number of nucleation sites triggering solidification.

In a nutshell, the present study shows, for the first time, the formation and stability of multiphase alloy nanoparticles embedded in Al matrix using MA.

ELECTRONIC SUPPLEMENTARY MATERIAL

REFERENCES

1. R. Goswami and K. Chattopadhyay: *Acta Metall.*, 1995, vol. 43, pp. 2837–47.
2. Q.S. Mei and K. Lu: *Prog. Mater. Sci.*, 2007, vol. 52, pp. 1175–262.
3. A. Singh and A. Tsai: *J. Phys.*, 2008, vol. 20, pp. 3140021–212.
4. S.K. Kang and S. Purushothaman: *J. Electron. Mater.*, 1999, vol. 28, pp. 1314–18.
5. E. Johnson, A. Johansen, L. Sarholt, and U. Dahmen: *J. Metastable Nanocryst. Mater.*, 2001, vols. 360–362, pp. 267–74.
6. E. Johnson, A. Johansen, C. Nelson, and U. Dahmen: *J. Electron Microsc.*, 2002, vol. 51, pp. S201–09.
7. P. Bhattacharya, V. Bhattacharya, and K. Chattopadhyay: *J. Mater. Res.*, 2002, vol. 17, pp. 2875–83.
8. P. Bhattacharya and K. Chattopadhyay: *Int. J. Nanosci.*, 2005, vol. 4, pp. 909–20.
9. V. Bhattacharya, E. Yamasue, K.N. Ishihara, and K. Chattopadhyay: *Acta Mater.*, 2005, vol. 53, pp. 4593–603.
10. S. Hagège and U. Dahmen: *Philos. Mag. Lett.*, 1996, vol. 74, pp. 259–66.
11. V. Bhattacharya, K. Chattopadhyay, and P. Ayyub: *Phil. Mag. Lett.*, 2005, vol. 85, pp. 577–85.
12. P.Y. Khan and K. Biswas: *J. Nanosci. Nanotechnol.*, 2015, vol. 15, pp. 309–16.
13. K. Biswas, P.Y. Khan, A. Singh, and A.P. Tsai: in *Proc. Process Fabr Adv Mater*-XVII, N. Bhatnagar and T. Srivatsan, eds., 2009, pp. 109–21.
14. A. Singh and A.P. Tsai: *Scripta Mater.*, 2001, vol. 44, pp. 2005–08.
15. P.Y. Khan and K. Biswas: *Philos. Mag.*, 2014, vol. 94, pp. 1–15.
16. H.W. Sheng: *Philos. Mag. Lett.*, 1996, vol. 73, pp. 179–86.
17. H.W. Sheng, K. Lu, and E. Ma: *Nanostruct. Mater.*, 1998, vol. 10, pp. 865–73.
18. D. Zhang and H. Walker: *Mater. Sci. Eng. A*, 2004, vol. 375, pp. 985–91.
19. S. Chithra, S. Lele, and K. Chattopadhyay: *Acta Mater.*, 2011, vol. 59, pp. 2009–19.
20. P. Villars and L.D. Calvert: *Pearson's Handbook of Crystallographic Data for Intermetallic Phases*, 2nd ed., ASM International, Ohio, 1991.
21. B.D. Cullity and S.R. Stock: *Elements of X-Ray Diffraction*, 3rd ed., Prentice Hall, Upper Saddle River, NJ, 2001.
22. H.P. Klug and L.E. Alexander: *X-ray Diffraction Procedures*, 2nd ed., Wiley, New York, 1974.
23. P.Y. Khan, V. Bhattacharya, K. Biswas, and K. Chattopadhyay: *J. Nanopart. Res.*, 2013, vol. 15, pp. 1–16.
24. K. Chattopadhyay and R. Goswami: *Prog. Mater Sci.*, 1997, vol. 42, pp. 287–300.
25. K.I. Moore, D.L. Zhang, and B. Cantor: *Acta Metall.*, 1990, vol. 38, pp. 1327–42.
26. W.T. Kim and B. Cantor: *J. Mater. Sci.*, 1991, vol. 26, pp. 2868–78.
27. A.K. Malhotra and D.C. Van Aken: *Philos. Mag. A*, 1995, vol. 71, pp. 949–64.
28. H.J. Fecht: *Nature*, 1992, vol. 356, pp. 133–35.
29. F.A. Mohamed: *Acta Mater.*, 2003, vol. 51, pp. 4107–19.
30. P.J. Miller, C.S. Coffey, and V.F. DeVost: *J. Appl. Phys.*, 1986, vol. 59, pp. 913–16.
31. R.B. Schwarz and C.C. Koch: *Appl. Phys. Lett.*, 1986, vol. 49, pp. 146–48.
32. M. Abdellaoui and E. Gaffet: *J. Alloy. Comp.*, 1994, vol. 209, pp. 351–61.
33. N. Hamada, M. Hamada, T. Uesugi, Y. Takigawa, and K. Higashi: *Mater. Trans.*, 2010, vol. 51, pp. 1747–52.
34. G.F. Bolling, L.E. Hays, and H.W. Wiedersich: *Acta Metall.*, 1962, vol. 10, pp. 185–94.
35. C. Suryanarayana: *Prog. Mater Sci.*, 2001, vol. 46, pp. 1–184.
36. T.D. Shen and C.C. Koch: *Acta Mater.*, 1996, vol. 44, pp. 753–61.
37. T.B. Massalski: *Binary Alloy Phase Diagram*, 2nd ed., ASM International, Park City, 1992.

38. D.L. Zhang and H. Walker: *Mater. Sci. Eng. A*, 2004, vols. 375–377, pp. 985–91.
39. M. Zhu, X.Z. Che, Z.X. iI, J.K.L. Lai, and M. Qi: *J. Mater. Sci.*, 1998, vol. 33, pp. 5873–81.
40. A.R. Yavari, P.J. Desre, and T. Benameur: *Phys. Rev. Lett.*, 1992, vol. 68, pp. 2235–38.
41. V. Bhattacharya and K. Chattopadhyay: *Acta Mater.*, 2004, vol. 52, pp. 2293–304.
42. K. Biswas, R. Galun, B.L. Mordike, and K. Chattopadhyay: *Metall. Mater. Trans. A*, 2005, vol. 36A, pp. 1947–64.
43. E. Ma, J.H. He, and P.J. Schilling: *Phys. Rev. B*, 1997, vol. 55, pp. 5542–45.
44. P. Bellon and R.S. Averback: *Phys. Rev. Lett.*, 1995, vol. 74, pp. 1819–22.
45. F.R. Mollard and M.C. Fleming: *Trans. Metall. Soc. AIME*, 1967, vol. 239, p. 1534.
46. K.G. Davis and L.M. Hogan: *J. Aust. Inst. Metals*, 1970, vol. 15, p. 29.
47. K.G. Davis and P. Fryzuk: *Canad. Met. Quart.*, 1971, vol. 10, p. 273.
48. W.J. Xie, C.D. Cao, Y.J. Lü, and B. Wei: *Phys. Rev. Lett.*, 2002, vol. 89, pp. 104304–8.
49. P. Adeva, G. Caruana, O.A. Ruano, and M. Torralba: *Mater. Sci. Eng., A*, 1995, vol. 194, pp. 17–23.
50. K. Lu and Z.H. Jin: *Curr. Opin. Solid St. M.*, 2001, vol. 5, pp. 39–44.
51. A. Singh and A.P. Tsai: *Sadhana*, 2003, vol. 28, pp. 63–80.